



Article

A Novel Algorithm of Haze Identification Based on FY3D/MERSI-II Remote Sensing Data

Yidan Si ^{1,2,3}, Lin Chen ^{1,2,3} , Zhaojun Zheng ^{1,2,3} , Leiku Yang ⁴ , Fu Wang ^{5,6}, Na Xu ^{1,2,3} and Xingying Zhang ^{1,2,3,*}

¹ National Satellite Meteorological Center, China Meteorological Administration, Beijing 100081, China

² Key Laboratory of Radiometric Calibration and Validation for Environmental Satellites, National Satellite Meteorological Center (National Center for Space Weather), China Meteorological Administration, Beijing 100081, China

³ Innovation Center for FengYun Meteorological Satellite (FYSIC), Beijing 100081, China

⁴ School of Surveying and Land Information Engineering, Henan Polytechnic University, Jiaozuo 454003, China

⁵ CMA Earth System Modeling and Prediction Centre (CEMC), Beijing 100081, China

⁶ State Key Laboratory of Severe Weather (LaSW), Beijing 100081, China

* Correspondence: zxy@cma.gov.cn; Tel.: +86-010-68408385

Abstract: Since 2013, frequent haze pollution events in China have been attracting public attention, generating a demand to identify the haze areas using satellite observations. Many studies of haze recognition algorithms are based on observations from space-borne imagers, such as the Moderate Resolution Imaging Spectroradiometer (MODIS), the Visible Infrared Imaging Radiometer Suite (VIIRS) and the Advanced Himawari Imager (AHI). Since the haze pixels are frequently misidentified as clouds in the official cloud detection products, these algorithms mainly focus on recovering them from clouds. There are just a few studies that provide a more precise distinction between haze and clear pixels. The Medium Resolution Imaging Spectrometer II (MERSI-II), the imager aboard the FY-3D satellite, has similar bands to those of MODIS, hence, it appears to have equivalent application potential. This study proposes a novel MERSI haze mask (MHAM) algorithm to directly categorize haze pixels in addition to cloudy and clear ones. This algorithm is based on the fact that cloudy and clear pixels exhibit opposing visible channel reflectance and infrared channel brightness temperature characteristics, and clear pixels are relative brighter, and as well as this, there is a positive difference between their apparent reflectance values, at 0.865 μm and 1.64 μm , respectively, over bright surfaces. Compared with the Aqua/MODIS and MERSI-II official cloud detection products, these two datasets treat the dense aerosol loadings as certain clouds, possible clouds and possible clear pixels, and they treat distinguished light or moderate haze as possible clouds, possible clear pixels and certainly clear pixels, while the novel algorithm is capable of demonstrating the haze region's boundary in a manner that is more substantially consistent with the true color image. Using the PM_{2.5} (particle matter with a diameter that is less than 2.5 μm) data monitored by the national air quality monitoring stations as the test source, the results indicated that when the ground-based PM_{2.5} $\geq 35 \mu\text{g}/\text{cm}^3$ is considered to be haze days, the samples with the recognition rate that is higher than 85% accounted for 72.22% of the total samples. When PM_{2.5} $\geq 50 \mu\text{g}/\text{cm}^3$ is considered as haze days, 83.33% of the samples had an identification rate that was higher than 85%. A cross-comparison with similar research methods showed that the method proposed in this study had better sensitivity to bright surface clear and haze areas. This study will provide a haze mask for subsequent quantitative inversion of aerosol characteristics, and it will further exert the application benefits of MERSI-II instrument aboard on FY3D satellite.

Keywords: MERSI-II; haze; heavy aerosol; cloud; bright surface; distinguish



Citation: Si, Y.; Chen, L.; Zheng, Z.; Yang, L.; Wang, F.; Xu, N.; Zhang, X. A Novel Algorithm of Haze Identification Based on FY3D/MERSI-II Remote Sensing Data. *Remote Sens.* **2023**, *15*, 438. <https://doi.org/10.3390/rs15020438>

Academic Editor: Carmine Serio

Received: 18 November 2022

Revised: 30 December 2022

Accepted: 30 December 2022

Published: 11 January 2023



Copyright: © 2023 by the authors. Licensee MDPI, Basel, Switzerland. This article is an open access article distributed under the terms and conditions of the Creative Commons Attribution (CC BY) license (<https://creativecommons.org/licenses/by/4.0/>).

1. Introduction

According to the explicit provisions of the World Meteorological Organization, haze is defined as a day when the average visibility is less than 10 km, the average daily relative humidity is less than 80%, and other atmospheric haze days that can lead to low visibility, such as precipitation, are excluded (WMO, 2005). Haze particles are mainly composed of extremely small particles suspended in the air, such as dust, sulfate and nitrate, which are drier than fog and wetter than dust [1]. Due to the influence of the energy consumption structure, the air pollution in China has evolved into regional and complex air pollution. In recent decades, continuous high-intensity atmospheric haze pollution has swept across central and eastern China, which has aroused the attention of domestic scholars from all walks of life [2–4].

Using the discrete ground stations that are distributed in a small area, continuous observations over a short period of time are feasible to analyze the reasons for the formation of special pollution processes and the changing trend of the pollutants. For example, the AOD increases persistently during the daytime, and the diurnal variation varies from about 15% in summer to about 45% in winter based on thirty-three months of aerosol data in Beijing [5]. In addition, a severe haze occurred on 20–27 September 2011 in the megacity of Beijing [6] and several serious haze events in Beijing between January 1 and 1 February 2013 have been observed [7]. Further, the North China Plain was analyzed by Che et al. (2014) [8] and biomass burning impacted the haze pollution in the Yangtze River Delta, China [9]. Previous studies have focused on monitoring the process of haze events and the variation characteristics of the haze formation mechanism; the distribution and variations of the haze process have seldom been analyzed over continuous spatio-temporal scales. Subsequently, there have been some studies that have discussed the spatio-temporal characteristics of haze by using the products retrieved from satellites. For example, the AOD datasets from the Collection 6 enhanced Deep Blue algorithm of MODIS aboard the Terra and Aqua satellites, the UV Aerosol Index from Ozone Monitoring Instrument (OMI) on the Aura satellite, the vertical detection of Cloud-Aerosol Lidar and Infrared Pathfinder Satellite Observations (CALIPSO) and other data were jointly used to analyze the variation characteristics and occurrence frequency of regional haze when the AOD > 1.0, which basically stabilized at 70–90 days, which was one year after 2009 [10–12]. Although the AOD data retrieved by satellites is used to analyze the characteristics of haze variation, some cloud-contaminated hazy areas have no valid AOD retrievals, which means not all of the aerosol retrieval algorithms are suitable over the heavily polluted regions [13].

Cloud detection algorithms based on satellite remote sensing data are generally designed to generate a cloud mask as an the input for the downstream cloud-relevant, environmental and continental elements retrieval [14]. Many studies revealed that the operational cloud detection products developed by MODIS, VIIRS and AHI lack the ability to classify haze aerosols, differentiate the thick aerosol layer from the cloudy pixels and they include certain uncertainties in desert and non-desert transition areas [7,15,16]. In the MOD/MYD04 aerosol retrieval algorithms, fast cloud detection has been designed to combine the standard derivation of the reflectance at 0.47 μm and 1.38 μm to distinguish the cloud edge from the reflectance identification [17]. Considering that the texture characteristic of haze is smoother than that of clouds, the variance information of a matrix composed of 3×3 pixels at 0.412 μm and 0.47 μm is added to the VIIRS cloud identification to avoid identifying a haze as a cloud [18].

In order to improve the discrimination of the cloud detection algorithm, many scholars have performed in-depth analyses of the characteristics of haze pixels. For example, after analyzing the spectral characteristics of cloud, fog, haze and clear pixels in visible-near infrared and infrared channels based on MODIS data, Ge et al. (2016) selected multiple sensitive channels to calculate the threshold combination of the haze distribution, and further, they designed an automatic processing algorithm for haze detection [19]. Shang et al. (2014) used MODIS secondary products for multi-day sampling to compare the difference in the cloud amount, cloud phase and cloud top pressure during clear days and

heavy pollution conditions; a recognition algorithm combining the threshold values of these three parameters was established to distinguish the haze pixels from the cloud regions [20]. Based on VIIRS data, Wang et al. (2017) selected cloud, clear sky and haze areas from more than 200,000 pixels of eastern China through visual interpretation, and then, they determined the thresholds of these two variables by fitting the histograms of the standard deviation changes of the three targets at $0.412 \mu\text{m}$ and $0.47 \mu\text{m}$, respectively, thus finally establishing a fast cloud, haze and clear sky identification algorithm for AOD inversion [15]. Ackerman (1998) believed that haze has a smaller optical thickness compared to that of clouds and is distributed on the surface. The digital elevation model (DEM) was added to retain the clear pixels above higher altitude mountains [21,22]. By analyzing the radiation distribution characteristics of 36 bands of accurate and mis-detected cloud detection points from the MODIS satellite, a cloud detection correction algorithm for mis-detected cloud products in high pollution areas was constructed, which solved the problem of cloud over-identification from the perspective of studying cloud microphysical characteristics [7]. NDVI can be used not only to identify vegetation distribution, but it can also be used to identify clouds and clear skies. Yang (2022) found that the sample with $\text{NDVI} < 0.1$ were treated as inland water, which is the main reason why the MODIS DT aerosol retrieval algorithm filters out haze areas [23]. Based on FY3D/MERSI-II data, Yang (2022) added a reflectance value of $2.13 \mu\text{m}$, which is below 0.08, to this condition to recover the haze area for retrieval. This method was then adopted by the MODIS DT team to retrieve the haze area from MODIS [24].

In recent years, China's domestic satellite sensor detection technology has developed rapidly. The Fengyun series of satellites, which are resource satellites and ocean satellites, the Gaofen series of satellites, which are environmental satellites, etc., were launched successively, basically realizing the Earth observation system for multiple application fields, thus serving the business needs of various industries. As for the Fengyun satellite series, Fengyun 3 was successfully launched in May 2008 as a polar solar synchronous orbit satellite. After nearly ten years of development in FY-3A, FY-3B, FY-3C and FY-3D, the Fengyun 3 Earth Observation System has matured, and it is in the stage of stable operation [25]. In 2008, the first Moderate Resolution Spectral Imager (MERSI) on FY-3 indicated that domestic satellites could be used for the quantitative remote sensing inversion of land and ocean aerosols [26,27]. In November 2017, Fengyun 3D was once again equipped with an upgraded version of the MERSI instrument, providing a solid data source for aerosol inversion [28,29]. The MERSI load performance is comparable to that of MODIS, whose business products are relatively mature. The cloud detection products of MERSI-II are as same as those of MODIS, therefore, both lack of the ability to identify haze. For aerosol properties retrieval, the classifications of the MERSI-II operational cloud mask (MERSI-CLM) cannot meet the requirements, therefore, it is urgent to carry out research on the multi-elemental identification of cloudy, hazy and clear skies based on the MERSI load observation data at present.

It has always been a difficult problem to identify haze and clouds using satellite data because haze and clouds have similar optical and micro-physical properties, and it is difficult to distinguish them by using traditional threshold methods. Considering the effectiveness of the business products, the improved algorithm, preferably, does not rely on external data. Therefore, based on the difference of the spectral characteristics of cloud, haze and clear sky pixels, this paper proposes a parameter that is suitable for clear sky pixels on a bright surface according to the characteristics of the MERSI payload instrument. The spectral differences of many wavelengths were combined to construct a fusion identification method. Section 2 introduces the data and the algorithm principle adopted by the algorithm, and the recognition effect and accuracy evaluation of the algorithm is introduced in Section 3.

2. Materials and Methods

2.1. Study Domain

Our study area, which is bounded by latitudes of 0° and 60°N and longitudes of 60°~160°E, mostly covers China, Mongolia, Korea, Japan, Southeast Asia, India and other regions. Among them, eastern China and India are often affected by anthropogenic source emissions, resulting in the frequent occurrence of haze. In northwest China, such as in Xinjiang, Gansu and other regions, dust and bare soil cover the land, the main aerosol type is the sand dust type, the amount of anthropogenic emissions is relatively small and the atmosphere is relatively clean. The Tibetan Plateau, which is 5 km above sea level, has a typical polar plateau climate, and it is often covered by clouds. In general, the study area selected in this paper includes a haze area, a cloud area and a clear sky area, which is conducive to a more comprehensive analysis of the performance of the recognition algorithm.

2.2. Data Sources

2.2.1. FY3D/MERSI-II

The Medium Resolution Imaging Spectrometer is one of the main optical imaging payloads on the FY-3 series satellites. The second generation of MERSI (MERSI-II) has been improved in its performance compared to that of the first generation, forming a double satellite network with the FY-3C series, which greatly improves China's meteorological satellite observation capability. MERSI-II uses multiple probes (10 or 40) and provides an image of about 2900 km (cross track) × 10 km (along track) per scan. Compared with MERSI-I, MERSI-II has 19 solar reflection channels and 1 infrared emission channel, which is equipped with a total of twenty-five channels, including sixteen visible-near infrared channels, three short-wave infrared channels and six medium-long wave infrared channels. Among them, six channels have a sub-satellite point resolution of 250 m, and the remaining nineteen channels have a resolution of 1000 m. The bands used in this study are listed in Table 1. The MERSI-II L1 data used in this study can be downloaded from the website <http://satellite.nsmc.org.cn/portalsite/default.aspx>. (accessed on 10 April 2022).

Table 1. The wavelengths of the FY3D/MERSI-II instrument used in the study.

Band	Center Wavelength (μm)	Width (nm)	Spatial Resolution (m)
1	0.47	50	250
2	0.55	50	250
3	0.65	50	250
4	0.865	50	250
5	1.38	50	250
6	1.64	50	1000
7	2.13	50	1000
12	0.67	20	1000
15	0.865	20	1000
19	1.03	20	1000
20	3.8	180	1000
24	10.8	1000	250

The MERSI-II operational cloud detection products were also downloaded from the above website, including a granular version and daily versions. The cloud mask products using the daily scale at a resolution of 1 km × 1 km and 5 km × 5 km were released at the same time, and this study adopted the data of the finer resolution one for the cross-comparison. The parameter named CLM_DAILY_D was extracted, and the values were

represented in bits and bytes for certainly the cloudy, probably cloudy, probably clear, certainly clear, coastal, sun glint and snow/ice areas. Considering that only the pixels over land were identified in this study, the pixels labeled as sun glint were treated as invalid filling values.

2.2.2. Aqua/MODIS

Two MODIS sensors were placed onboard the EOS Terra and EOS Aqua satellites. Terra/MODIS and Aqua/MODIS have been in orbit for more than 20 years, providing indispensable data sources for global and regional air quality monitoring, special weather events, urbanization development, assimilation systems and climate change, etc. [30–34]. Since FY3D is an afternoon satellite, the MYD35 cloud products with a resolution of 1 km² based on Aqua were selected for the evaluation, thus minimizing the inconsistency between the MERSI and MODIS mis-identification results over the time period. The meaning of the values in the dataset are as same as those of MERSI-II.

2.2.3. Auxiliary Datasets

The identification of haze pixels based on satellite remote sensing data is still in the research stage, and the corresponding official products have not released yet, therefore, there are still great difficulties in quantitative validation of haze recognition. The real-time PM_{2.5} monitoring data released by the national ground air quality monitoring stations can be taken as the true ground-based observation values, which usually reflect the air quality conditions at the stations, and the larger the value is, then the more serious the pollution is. There were 1670 monitoring stations nationwide on 22 October 2020. As shown in Figure 1, most of the stations are located in eastern China, with a few in the Xinjiang and Yunnan provinces [35]. The Ministry of Environmental Protection classifies the value of PM_{2.5} into six ranks, with a value below 35 µg/m³ being excellent, a value larger than 35 µg/m³ and smaller than 75 µg/m³ (define as 35~75) being good, a value of 75 µg/m³~115 µg/m³ being classified as mild pollution, a value of 115 µg/m³~150 µg/m³ being classified as moderate pollution, a value of 150 µg/m³~250 µg/m³ being classified as severe pollution and a value of larger than 250 µg/m³ being classified as serious pollution, which can be used as a data source to verify the identification accuracy of this study.

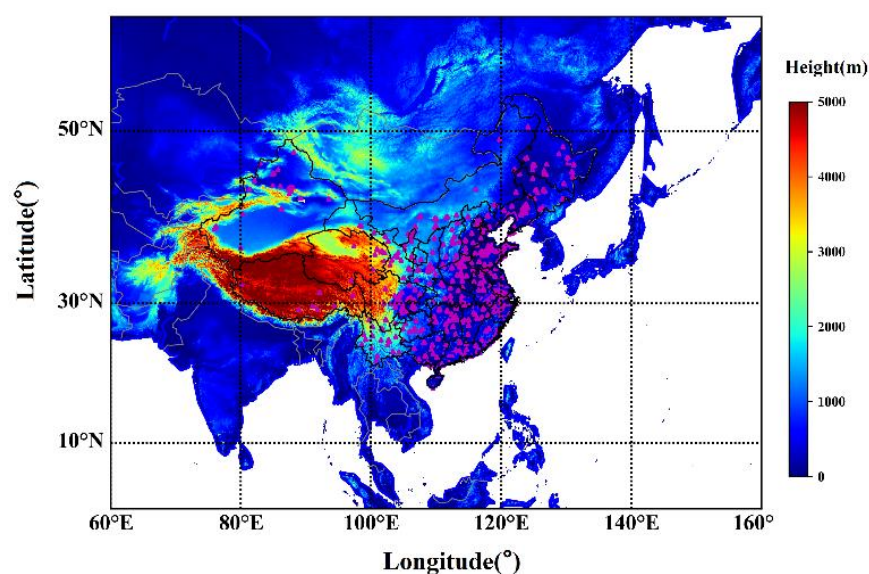


Figure 1. The study domain and overlapped digital elevation model from MERSI-II Level 1 GEO1K. The sea surface is shown in white. The national PM_{2.5} monitoring stations employed by the Ministry of Environmental Protection on 22 October 2020 are depicted as the magenta-colored dots.

Additionally, Yang (2022) mentioned in his research on aerosol retrieval using MERSI remote sensing data that some haze areas could be recovered by modifying the recognition conditions of inland water bodies [23]. In this paper, the method proposed by Yang (2022) were replicated and cross-compared with the results of this study.

2.3. MHAM Algorithm

2.3.1. Algorithm Description

The design of the MHAM algorithm builds upon the spectral characteristics of different pixels, for example, the reflectance of the cloud pixels in the visible band is greater than that of the clear sky pixels, while the brightness temperature in the infrared channel is usually lower than that of the clear sky and haze pixels, and the brightness temperature difference is also higher than that of the clear sky and haze pixels. The reflectivity ratio of the near-infrared channel and the visible channel (such as the ratio of $R_{0.865}$ and $R_{0.65}$) has different values in different underlying surfaces [19,20,22]. The above characteristics were taken as the prior knowledge of this algorithm, and the adaptive improvements to the threshold selection were carried out for the MERSI instrument. Based on the selected MERSI bands, the tests were divided into two groups to distinguish the cloud, clear and haze pixels from each other. The flowchart of the algorithm is shown in Figure 2.

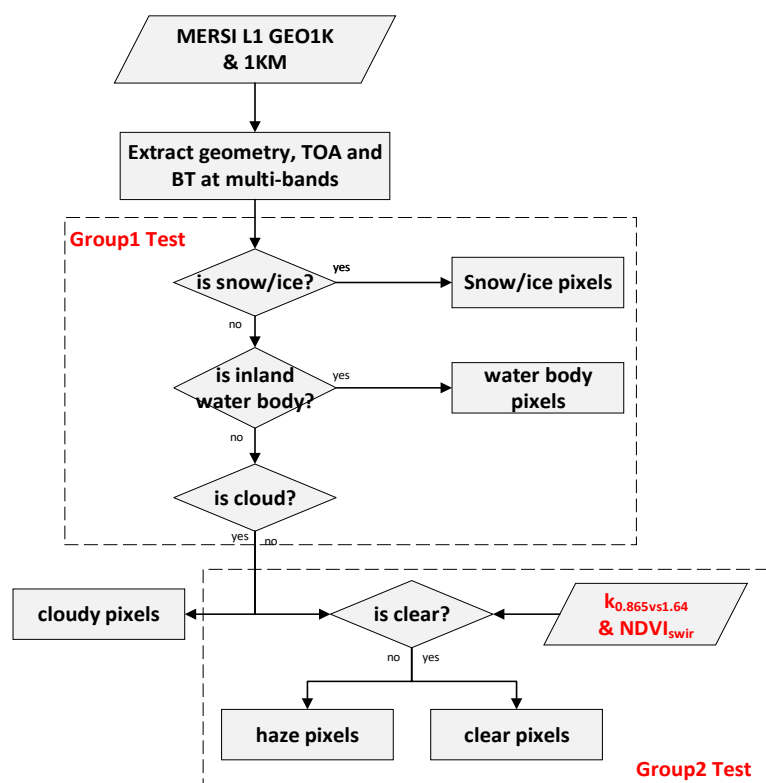


Figure 2. Flowchart of the MHAM algorithm using FY3D/MERSI-II observations.

Firstly, the DN (data number) values at different bands were extracted from the MERSI-II L1 data and converted to the apparent reflectance of the top of the atmosphere (TOA) at visible wavelengths or the brightness temperature at the infrared bands. The geolocation information and observed angles were extracted from the dataset. It must be noted that the MERSI Level 1 data at 1 km instead of those at 250 m were used in this analysis. Secondly, the ice/snow pixels were filtered out using the normalized difference snow index (NDSI), which was calculated using the apparent reflectance values at $0.55 \mu\text{m}$ ($R_{0.55}$) and $1.64 \mu\text{m}$ ($R_{1.64}$) for Landsat or $R_{0.55}$ and $R_{2.12}$ for MYD35 or $R_{0.865}$ and $R_{1.24}$ for MXD04 DT. Here, the ratio of the difference between $R_{0.55}$ and $R_{1.64}$ to the sum of $R_{0.55}$ and $R_{1.64}$ was taken as the NDSI. When both $\text{NDSI} > 0.4$ and $R_{0.865} > 0.1$ were true, the pixel was

treated as it was ice/snow. The inland water was identified by the combined conditions of the NDVI and $R_{2.13}$. For the remaining pixels, $R_{0.65}$, BT_{11} and the standard derivation of $R_{0.47}$ were used together for distinguishing the cloud pixels. Based on the binary tree method, the cloud and non-cloud pixels were, respectively, determined. Combined with the actual characteristics of the MERSI data, clear pixels over brighter surfaces can be captured accurately by introducing the variation between $R_{0.865}$ and $R_{1.64}$. In addition to the lower reflectance and higher brightness temperature values of the clear areas, the clear pixels and the remaining haze regions can be separated. More details about the conditions are summarized in Table 2.

Table 2. Details thresholds for MHAM algorithm using FY3D/MERSI-II observations.

Classification	Group1	Group2
ice/snow	¹ $NDSI > 0.4 \ \& \ R_{0.865} > 0.1$	/
Inland waterbody	² $NDVI_{nir} < 0.4 \ \& \ R_{2.13} < 0.08$	/
cloud	$R_{0.65} > 0.45$ [defined as cloud_c1]	/
	$R_{0.47_std} > 0.0075 \ \& \ R_{0.65} > 0.4$ [defined as cloud_c2]	
	$BT_{11} < 250 \text{ K}$ [defined as cloud_c3]	
clear	/	$0 < R_{0.65} < 0.2$ [defined as clear_c1]
		$Diff_{0.865_1.64} > 0$ [defined as clear_c2]
		$BT_{11} > 285$ [defined as clear_c3]
		$BT_{11} - BT_{3.8} \in [-50, -40]$ [defined as clear_c4]
		³ $NDVI_{swir} < 0.2 \ \& \ 0.2 \leq R_{0.65} < 0.4$ [defined as clear_c5]

¹ $NDSI = (R_{0.55} - R_{1.64}) / (R_{0.55} + R_{1.64})$; ² $NDVI_{nir} = (R_{0.865} - R_{0.65}) / (R_{0.865} + R_{0.65})$; ³ $NDVI_{swir} = (R_{0.865} - R_{0.65}) / (R_{0.865} + R_{0.65})$.

2.3.2. Selection of Spectral Characterization Based on FY3D/MERSI-II

In this analysis, the apparent reflectance at $0.65 \ \mu\text{m}$ ($R_{0.65}$), the brightness temperature at $11 \ \mu\text{m}$ (BT_{11}) and the difference between BT_{11} and $BT_{3.8}$ ($BT_{11} - BT_{3.8}$) were selected to separate the cloudy and clear skies according to different thresholds. It should be emphasized that $0.65 \ \mu\text{m}$ of atmospheric passage was selected in this paper, instead of using $0.47 \ \mu\text{m}$ of it, as was used in the MODIS aerosol algorithm. This is because the molecular scattering contribution is larger at large observation angles, and the apparent reflectance of clear sky pixels is larger than that of some haze pixels. Assuming that the solar zenith angle is 30° , the relative azimuth is 72° , the aerosol model is defined as the continental aerosol type in the mid-latitude summer and the satellite zenith angle ranges from 0 to 80° , Figure 3a,b presents the variation of molecular scattering under different aerosol loadings with the satellite zenith angles. When the observed angles are smaller than 50° , the contribution of molecular scattering changes modestly, whereas the molecular scattering increases significantly when the satellite zenith angles change from 50° to 80° . The scattering amplitude of the molecules in the red channel is less than $1/3$ of that which occurs in the blue channel. The aerosol optical thickness decreases with the increase in the wavelength. As shown in Figure 3c,d, the variation trend of the aerosol scattering signal in the red band with observation angles is consistent with that of the blue band, and it is still sensitive to different aerosol contents. If $0.47 \ \mu\text{m}$ is used as the reflectance identification condition, it is easy to misidentify some clear sky pixels as haze ones. Therefore, it is feasible to select $0.65 \ \mu\text{m}$ as the identification condition in this paper.

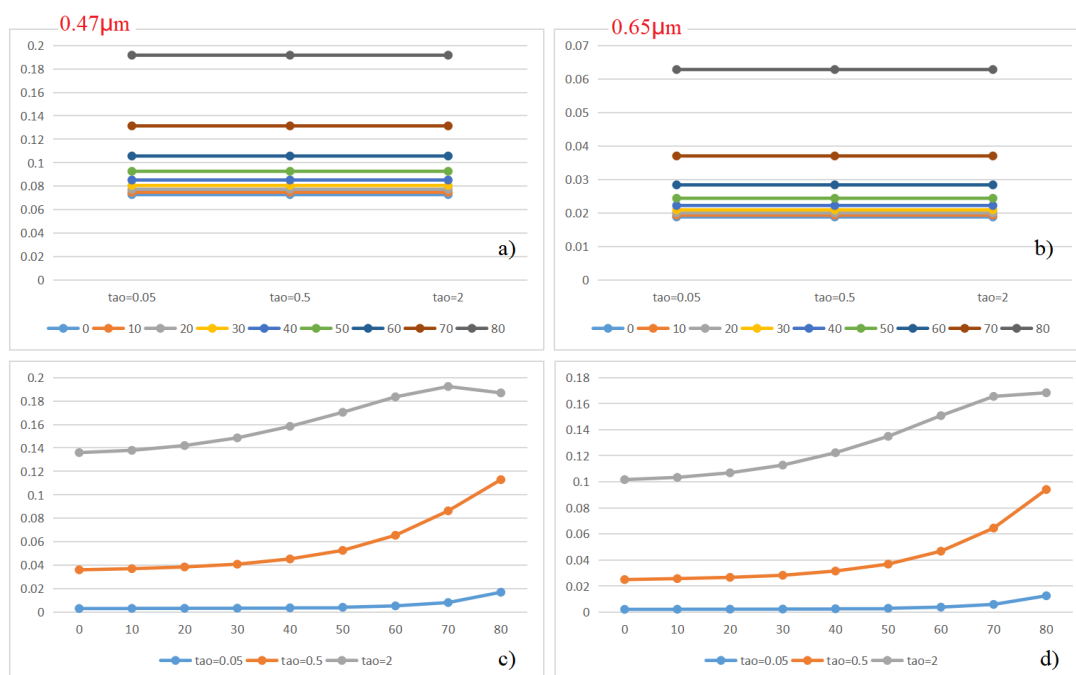


Figure 3. Variation of the apparent reflectance at two bands from molecule scattering (a,b) and aerosol scattering (c,d) as simulated by 6SV; the left panel stands for the variation in blue the channel, and the right one denotes in the red channel. Different colors in sub-panels (a,b) represent satellite zenith angles, and those in sub-panels (c,d) represent aerosol optical thickness.

2.3.3. Identification of Clear Conditions over Bright Surface

It is difficult to distinguish the clear pixels over the bright surface from the haze conditions due to them having similar spectral characteristics. The accuracy of haze detection could be heavily improved provided that the clear conditions over the bright surfaces can be accurately identified [21]. Through visual interpretation, the scenes of cloud, clear and haze regions on different underlying surfaces were selected, including spring, summer, fall and winter ones. The selected regions were kept constant to reduce the complexity of the scenes. The selected region changed only when the study region during a season was no longer pure. Details about the regions are summarized in Table 3. Inner Mongolia was selected as the clear region with a bright surface, which is defined as clear1. The area in Guangdong province was selected as clear2. The two cloud scenarios were selected to be located in Sichuan and Shaanxi, respectively. The Hebei and Henan provinces, where haze occurs frequently, were selected as the two haze scenarios. We extracted the apparent reflectance values at eight bands of each scenario, and we averaged them by region and season.

Figure 4 shows the variation trend of spectral reflectance in each scenario. A similar pattern appeared in two cloudy scenarios, but with different apparent reflectance values. The reflectance of different bands in clear2, the haze1 and haze2 showed similar variation. Surprisingly, in clear1, the apparent reflectance of the B6 and B7 channels are larger than those of the B4 and visible channels, which is contrary to that of the cloudy and haze pixels. Haze often contains absorptive components, which will attenuate the apparent reflectance after absorbing an amount of solar radiation. As we know, 1.64 μm and 2.13 μm were often used to study the characteristics of the parameters over land. For the clear pixels, 2.13 μm is only a little bit affected by the atmosphere, and the apparent reflectance is almost equal to the surface reflectance. Compared with 1.64 μm, the total apparent reflectance at 2.13 μm may be smaller than the surface reflectance with the enhancement of the atmospheric signal. As described as Section 2.3.1, visible wavelengths are susceptible to molecular scattering, therefore, the near-infrared channel (B4) and the B6 channel were selected to construct the reflectance variation for identifying the clear pixels over bright surfaces. Non-bright surface

clear skies (clear2) are usually well identified when one is using a reflectance value that is below a certain threshold. If the cloud pixel coverage area can be accurately identified, clear skies and haze can be distinguished from the remaining samples.

Table 3. The MERSI-II data set used for training the identification condition with bright surfaces.

Scenarios	Selected Areas	Selected Time
clear1	42.8496°~45.3657°, 109.1090°~113.6038°	8 November 2019/4 April 2020/ 14 June 2020
	42.2122°~43.1121°, 108.6515°~109.7193°	3 December 2019
clear2	23.9992°~24.3478°, 112.7604°~113.6705°	8 November 2019/3 December 2019
	23.0716°~23.7766°, 115.0593°~115.8996°	2 December 2019
	25.3634°~25.9159°, 116.7444°~117.5885°	15 March 2020
cloud1	27.8471°~29.0374°, 103.8887°~105.2329°	8 November 2019/23 December 2019/ 3 April 2020/17 June 2020
cloud2	36.1867°~36.7887°, 108.4950°~109.3658°	8 November 2019/24 December 2019/ 1 April 2020/22 June 2020
haze1	38.0390°~39.24°, 115.2247°~116.4105°	8 November 2019/13 December 2019/ 6 April 2020/11 June 2019
haze2	33.9950°~35.4849°, 113.6284°~114.8294°	8 November 2019/13 December 2019/ 26 April 2020/18 June 2020
	34.8348°~35.8514°, 114.2112°~115.4611°	18 June 2019

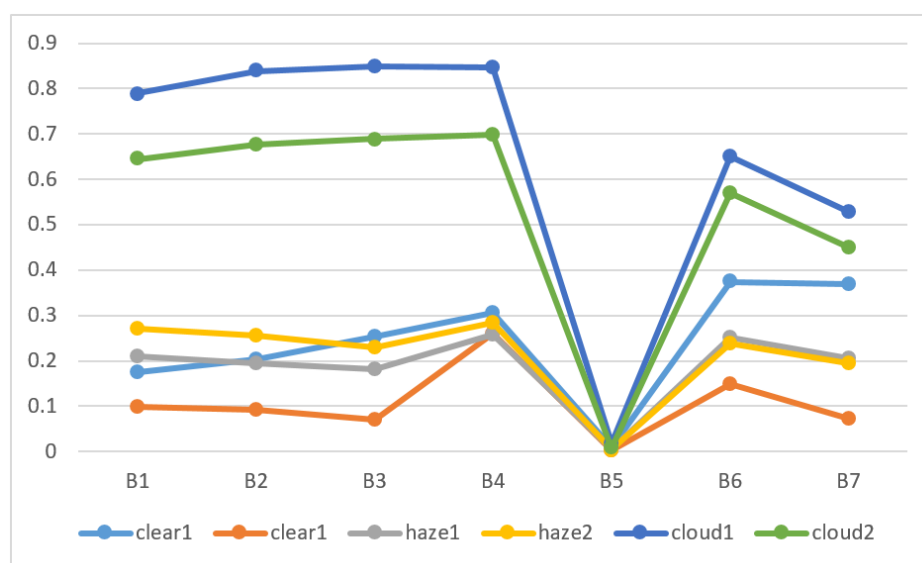


Figure 4. The spectral variation of different pixels over different underlying surfaces using MERSI-II apparent reflectance data. Different colors correspond to the scenarios in Table 2.

To confirm that whether the above parameter is reasonable, Figure 5 shows the difference of between $R_{0.865}$ and $R_{1.64}$ on 8 November 2019 and 1 December 2019, and a difference that is larger than 0 is masked in the white color. Combined with the true color maps, this parameter is sensitive to the clear sky with the bright surface. Therefore, this parameter can be added to the recognition process to further reduce the misjudgment of clear pixels over bright surfaces.

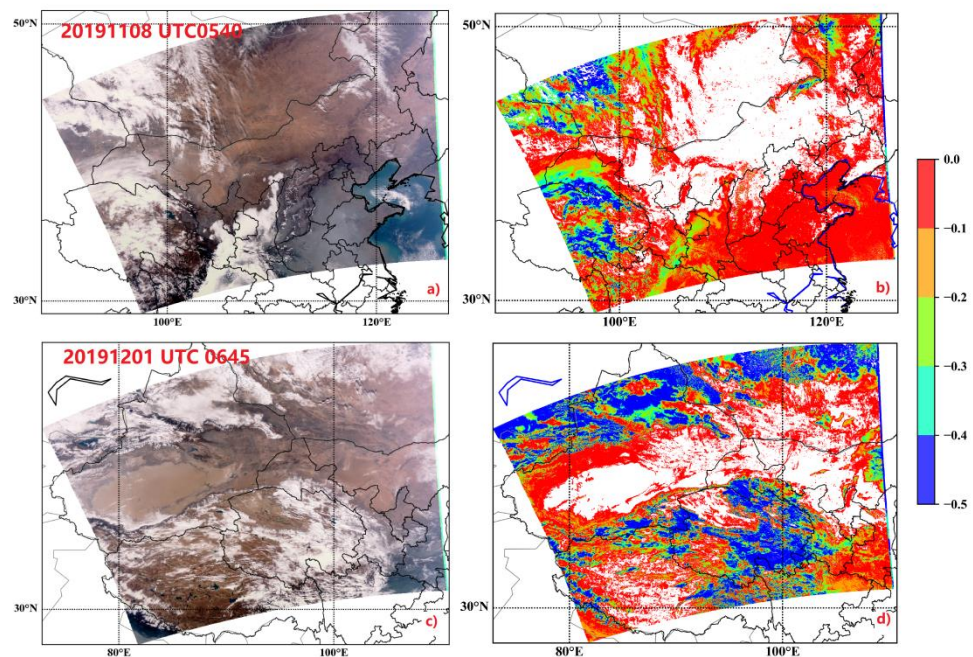


Figure 5. True color map and the distribution of the difference between $R_{0.865}$ and $R_{1.64}$. (a) True color map at UTC0540 on 8 November 2019; (b) the difference between $R_{0.865}$ and $R_{1.64}$ at UTC0540 on 8 November 2019; (c) True color map at UTC0645 on 1 December 2019; (d) the difference between $R_{0.865}$ and $R_{1.64}$ at UTC0645 on 1 December 2019.

2.3.4. Single Threshold Tests

Cloud Threshold Tests

$R_{0.65}$ is an effective indicator of clouds with large reflectance and small absorption values. BT_{11} is helpful for detecting cold clouds over inland water and certain land features. As mentioned above, the standard derivation of the reflectance at $0.47 \mu\text{m}$ usually stands for the texture patterns of the cloud edge. The cloudy regions detected using the detection conditions are shown in Figure 6. It should be addressed that Figure 6b–d intends to show that these three conditions were not independent when we were detecting cloudy pixels and the common regions distinguished by the three conditions were overwritten by the latter condition. This test of $R_{0.65}$ (defined as cloud_c1) was very robust over bright cloud layers, but it was invalid over very thin cirrus and cloud boundaries. The cloud_c2 is sensitive to the cloud edges that cloud_c1 did not detect. Part of the cloudy regions over the ocean were captured by cloud_c3, which was not detected by cloud_c1 nor cloud_c2. The complete cloudy regions exhibited in Figure 6e complement each other, showing that each criterion is necessary.

Clear Threshold Tests

As mentioned above, the red channel is less affected by molecular scattering than the blue channel is, therefore, $R_{0.65}$ can be also used to identify the pixels over an absolutely clear sky. We assumed that a pixel is treated as clear when $R_{0.65} < 0.2$, as shown in Figure 7b. Based on the actual characteristics of the MERSI data, it is found that the difference between $R_{0.865}$ and $R_{1.64}$ can be an indicator of distinguishing the clear pixels on a bright surface. As depicted in Figure 7c, the clear sky areas in Inner Mongolia, northwest Lanzhou and part of Qinghai were accurately identified. In addition, there are few atmospheric signals in Shanxi and Hebei that had been captured by this condition. BT_{11} is also used as a clear sky identification condition. Through trial and error, when $BT_{11} > 285 \text{ K}$, it is considered as a clear sky pixel, as shown in Figure 7d. It can be seen that the bright temperature difference between BT_{11} and $BT_{3.9}$, the reflectance between 0.2 and 0.4 and $NDVI_{\text{swir}} < 0.2$ are a supplement to the bright surface clear sky area. Using these three cloudy conditions

and five clear sky conditions, the remaining pixels marked in white in Figure 7g were identified as haze pixels.

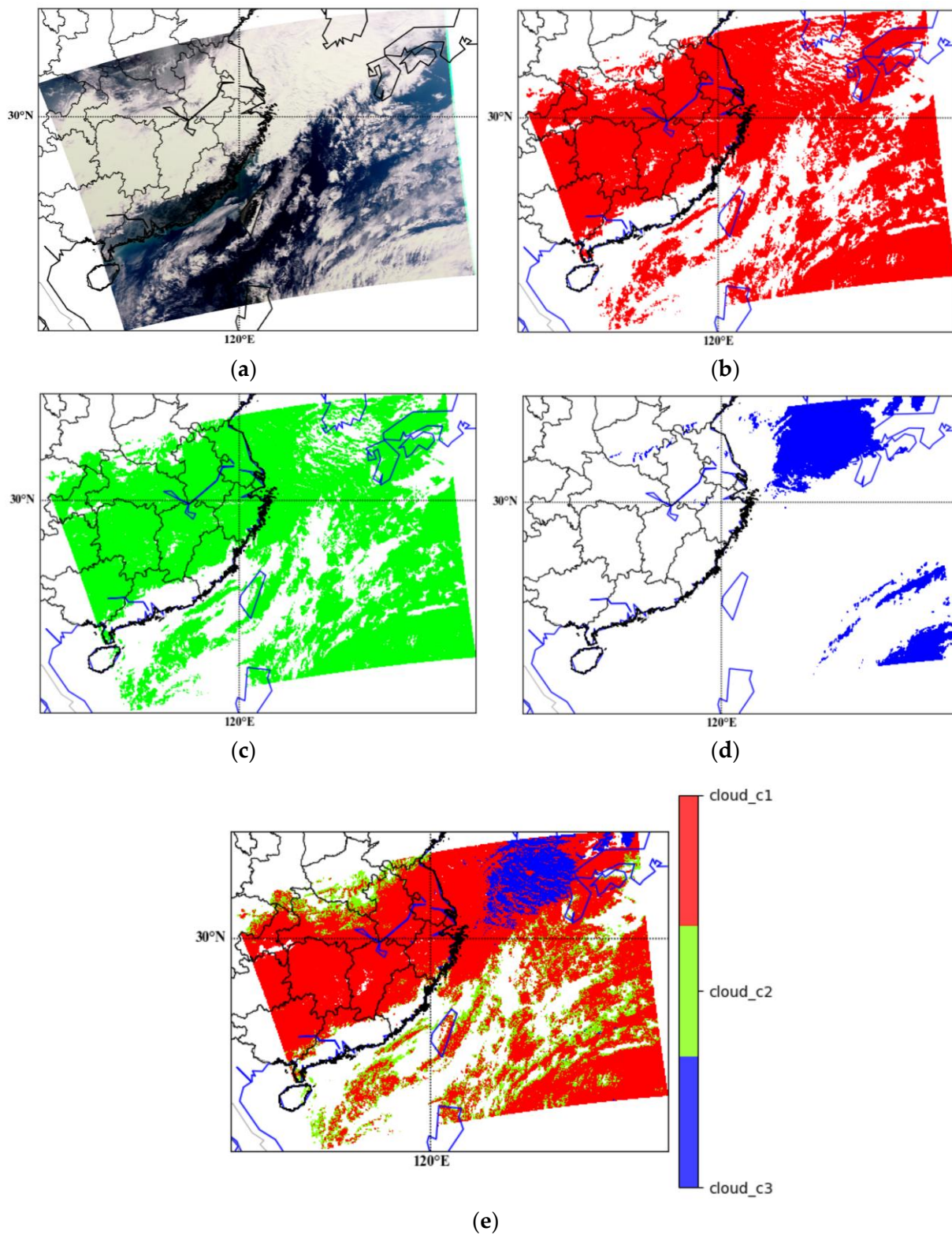


Figure 6. Test of cloud detection conditions at UTC0500 on 1 December 2019. (a) A true color map. (b) The cloudy region was detected by cloud condition 1, (c) the cloudy region was detected by cloud condition 2, (d) the cloudy region was detected by cloud condition 3 (e) and the final cloudy regions were detected by three conditions.

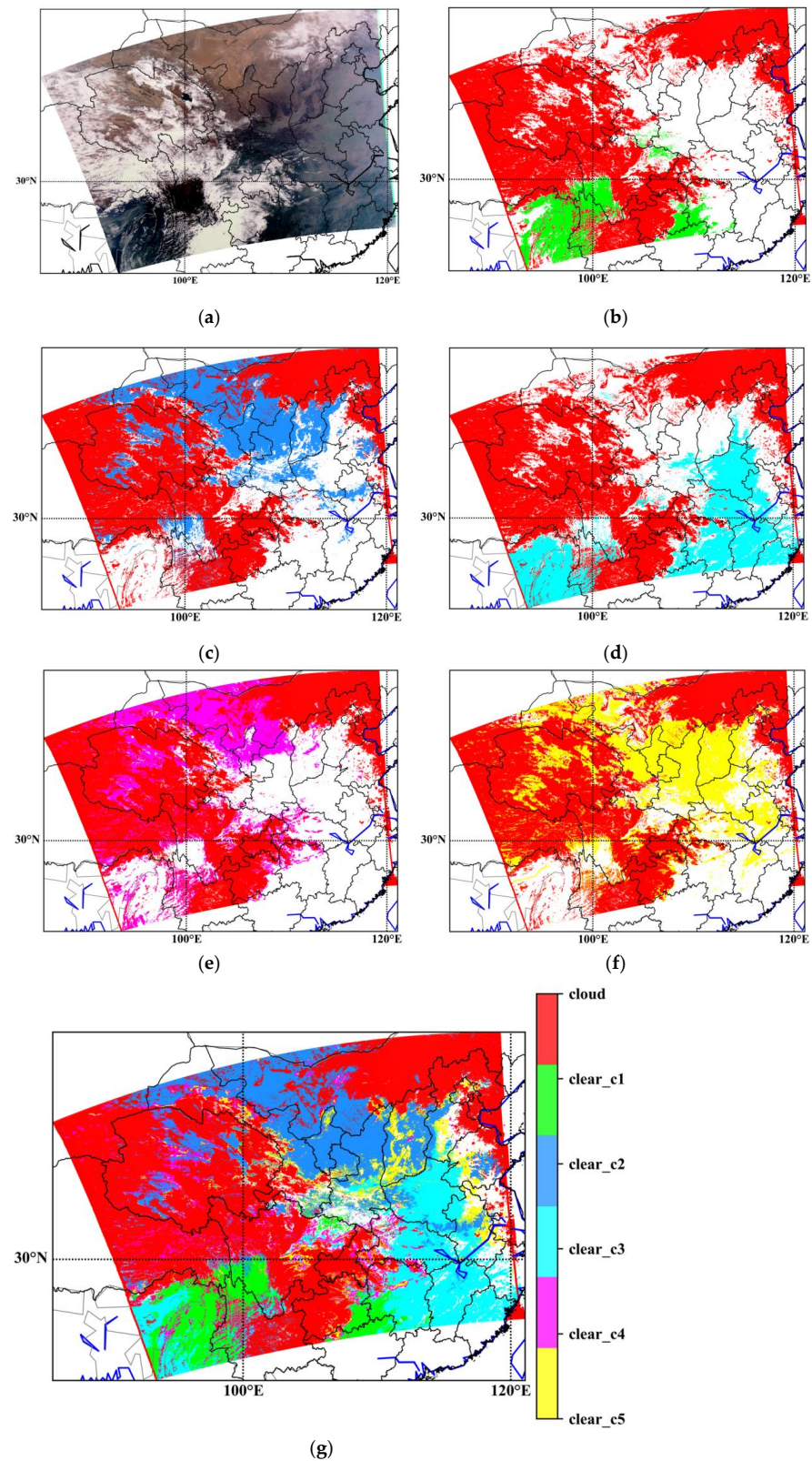


Figure 7. Test of clear detection conditions at UTC0605 on 3 December 2019. (a) A true color map. (b) The cloudy region was detected by three cloud conditions and the first clear condition, (c) the clear pixels were detected by clear condition 2, (d) the clear pixels were detected by clear condition 3, (e) the clear pixels were detected by clear condition 4, (f) the clear pixels were detected by clear condition 5 and (g) the final cloudy regions and clear pixels were detected by three cloudy conditions and five clear conditions.

3. Results

3.1. Distribution of Haze Identification

Two haze scenarios in winter were selected to test the performance of our proposed method, as shown in Figure 8. The first row of images is 2 December 2019, and the second row is 9 February 2020. The left panel is a true color map, and the right one is the distribution of the identified haze. On 2 December 2019, most parts of eastern China and India were shrouded by haze. Except for the clear sky area in Inner Mongolia, Xinjiang and the Qinghai-Tibet Plateau, the other parts of the whole study area were covered by cloud pixels. All of the above phenomena could be identified by the algorithm, and the boundary between the clear sky area and the cloud area could be clearly identified by the algorithm. According to the true color map, on 9 February 2020, the haze in the eastern coastal areas of China, such as Shandong and Tianjin, was relatively serious, while other areas were basically experiencing the state of light haze. In India, medium haze and light haze appeared simultaneously, and the distribution of clouds, clear skies and haze were also accurately identified. However, it is easy to miss cloud features when a thin or broken cloud covers a clear sky (e.g., South Korea and North Korea), and there is a slight error in distinguishing light haze from clear sky (e.g., Central India).

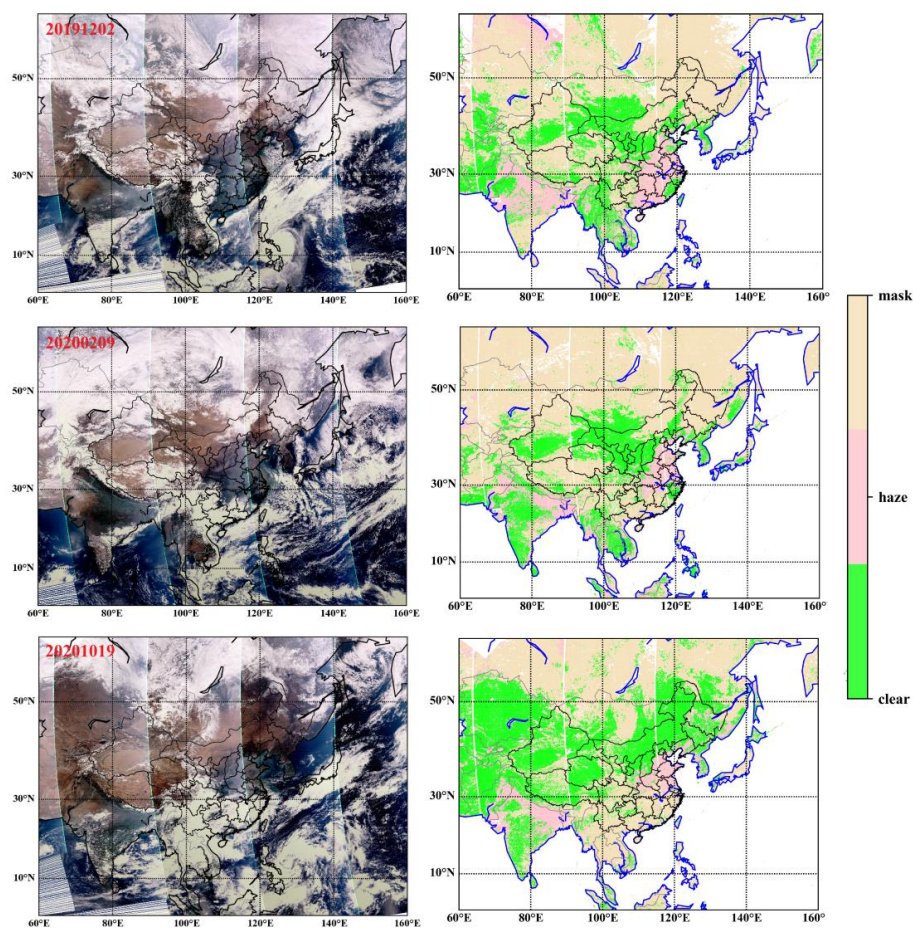


Figure 8. True color map and corresponding identification map based on MHAM algorithm, these three rows represent the distributions on 2 December 2019, 9 February 2020 and 19 October 2020, respectively.

In addition, the performance of clear pixels on a brighter surface in 19 October 2020 is further presented as the third row of images in Figure 8. Compared with the true color map, it can be clearly seen that the algorithm can accurately identify the clear sky pixels in high-altitude areas such as Inner Mongolia, northwest China, Afghanistan, Pakistan and

the Qinghai-Tibet Plateau, as well as the clear sky in low-value areas of the three provinces of northeastern China. It shows that the variation of 0.865 and $1.64 \mu\text{m}$ and $\text{NDVI}_{\text{swir}}$ introduced in this algorithm are effective.

Meanwhile, the corresponding operational cloud mask with the same dates as Figure 8 derived from MYD35 and MERSI-II were also presented for a cross-comparison. As depicted in Figure 9, the cloud, probably cloud, clear and probably clear pixels are drawn in yellow, gray, green and aqua, respectively. The recognition values of the clear sky and cloud pixels are basically the same, and the difference is mainly reflected in the processing of possible cloud and possible clear sky pixels. Compared with the classifications in Figure 8, neither the MODIS nor MERSI-II operational cloud mask identified the haze regions that appeared in India and in eastern China. It can be seen that MODIS treated those as probably cloud and probably clear pixels, while the processing conditions of MERSI-II were not as strict as that of MODIS, thus most of the haze pixels were labeled as clear.

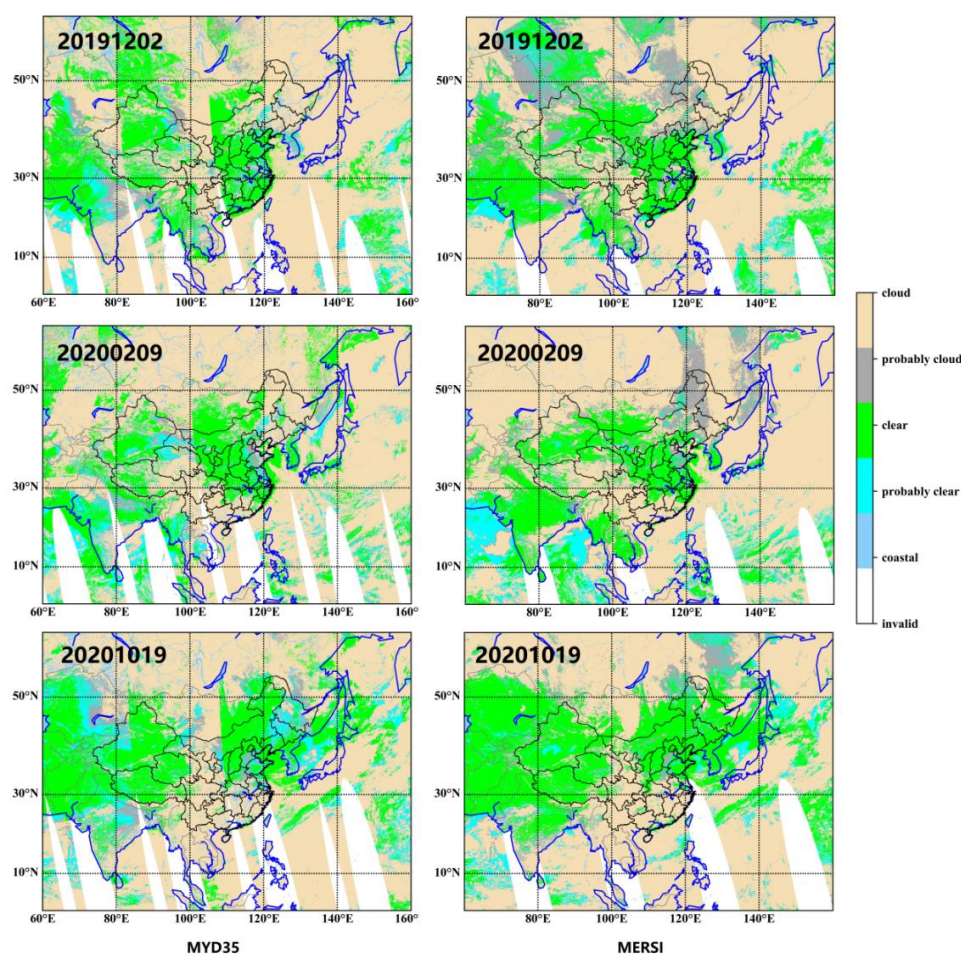


Figure 9. Aqua/MODIS cloud mask (left) and MERSI operational cloud mask (right), these three lines represent the distribution on 2 December 2019, 9 February 2020 and 19 October 2020, respectively.

3.2. Validation against $\text{PM}_{2.5}$ Measurements

As we all know, ground-based stations measure the air quality near the surface, while satellites observe the overall state in the troposphere. There are differences between these observation methods. At present, there is no unified standard, that is, when the $\text{PM}_{2.5}$ values measured by ground observation are greater than the threshold, it is consistent with the haze determined by the satellite. Therefore, this paper uses the two thresholds of $35 \mu\text{g}/\text{m}^3$ and $50 \mu\text{g}/\text{m}^3$ of the existing $\text{PM}_{2.5}$ levels to test the MERSI haze identification effect.

Firstly, the 18 MERSI orbits covering eastern China during the haze season were selected, which were mainly concentrated at 12–14 PM Beijing time. The national observation

PM_{2.5} data during the same period were downloaded, and the samples with a PM_{2.5} that was larger than 35 µg/m³ and 50 µg/m³ were respectively screened out for validation. Secondly, the spatial and temporal matching between the ground-based and satellite observations was performed. In the terms of the temporal scale, we chose the PM_{2.5} value with the nearest hour to the MERSI orbit, for example, the transit time of MERSI is UTC0515, so we chose PM_{2.5} data at 13:00 Beijing time. Spatially, taking the national station as the center, the MERSI pixels falling within a radius of 500 m were selected. If there were multiple pixels, then the nearest one was selected. Thirdly, the pixels identified by MERSI as cloud, ice/snow, inland waterbody ones were further removed from the matched samples, and only the haze and clear pixels were retained. Finally, the ratio of the number of samples identified as haze to that of the sum of the samples identified as haze and clear pixels were calculated to demonstrate the accuracy. Table 4 summarizes the test results based on the selected MERSI orbits. As it can be obviously seen in Table 4, the haze identification rate with a PM_{2.5} threshold of 50 µg/m³ is generally better than that with a PM_{2.5} threshold of 35 µg/m³. When PM_{2.5} > 35 µg/m³ was considered to be haze days, 13 samples with an identification rate that was larger than 85% accounted for 72.22% of the total samples (18), and 61.11% of the sample points (11) had an identification rate that was above 90%. When ground-based PM_{2.5} > 50 µg/m³ was considered as haze days, 83.33% and 66.67% of the samples had identification rates that were higher than 85% and 90%, respectively, indicating that the greater the ground-based PM_{2.5} value is, the better the consistency is of the satellite identification of haze.

Table 4. Accuracy test of FY3D/MERSI-II haze identification effect based on ground air quality PM_{2.5} monitoring data.

Date/Orbit	PM _{2.5} >= 50 µg/m ³			PM _{2.5} >= 35 µg/m ³		
	Haze	Clear	Hit Rate (%)	Haze	Clear	Hit Rate (%)
14 January 2020-0430	48	2	96.00	76	5	93.83
19 January 2020-0435	163	2	98.79	195	6	97.01
20 January 2020-0555	145	42	75.94	190	66	74.21
28 January 2020-0505	201	33	85.90	250	39	86.51
29 January 2020-0445	172	11	93.99	220	18	92.44
30 January 2020-0425	74	2	97.37	86	4	95.56
31 January 2020-0545	162	15	91.53	242	28	89.63
31 January 2020-0550	129	61	67.89	139	91	60.43
3 February 2020-0450	125	5	96.15	198	18	91.67
9 February 2020-0435	95	0	100	144	2	98.63
4 March 2020-0520	53	0	100	94	1	98.95
4 March 2020-0525	14	2	87.5	12	33	26.67
7 March 2020-0425	83	1	98.81	98	2	98.0
7 March 2020-0430	10	0	100	12	12	100
19 October 2020-0445	136	5	96.45	193	12	94.15
21 October 2020-0545	64	11	85.33	5	46	9.80
21 October 2020-0550	1	26	3.70	127	34	78.88
22 October 2020-0525	91	5	94.79	164	15	91.62

Taking some orbits as an example, Figure 10 shows the true color map and the MERSI identification results overlapping it with the PM_{2.5} values that were observed by the national stations of UTC0505 on 20 January 2020, UTC0450 on October 19 and UTC0525 on October 22, respectively, covering the scenarios of cloudy, hazy and clear skies over

different surface types. For the MERSI identification results, cloud, snow, ice and inland water were combined into masks, and they are marked with yellow. For the pixels that MERSI identifies as clouds, no matter how large the $PM_{2.5}$ observed by the state-controlled stations was, they could not be captured (these stations are not hidden here). For the pixels identified as clear skies by MERSI, most of the overlapped $PM_{2.5}$ values were smaller than $35 \mu\text{g}/\text{m}^3$, such as the skies over Inner Mongolia and southern China on October 19. Due to its topography and large amount of anthropogenic emissions, haze events occur frequently in the North China Plain. From the true color map, it is obvious that the North China Plain was covered by haze on January 28, February 3 and October 19. This study can identify these haze areas well, and the superimposed $PM_{2.5}$ level is at least good. It should be emphasized that at UTC0525 on October 22, the haze pollution levels in the Henan, Anhui and Jiangsu Provinces were not obvious on the true color map, but these areas were identified as haze in this study. According to the observation data from the national control station, $PM_{2.5}$ was already in moderate and severe pollution. In general, the haze area and clear sky area identified by this study are consistent with the classification of the national control stations.

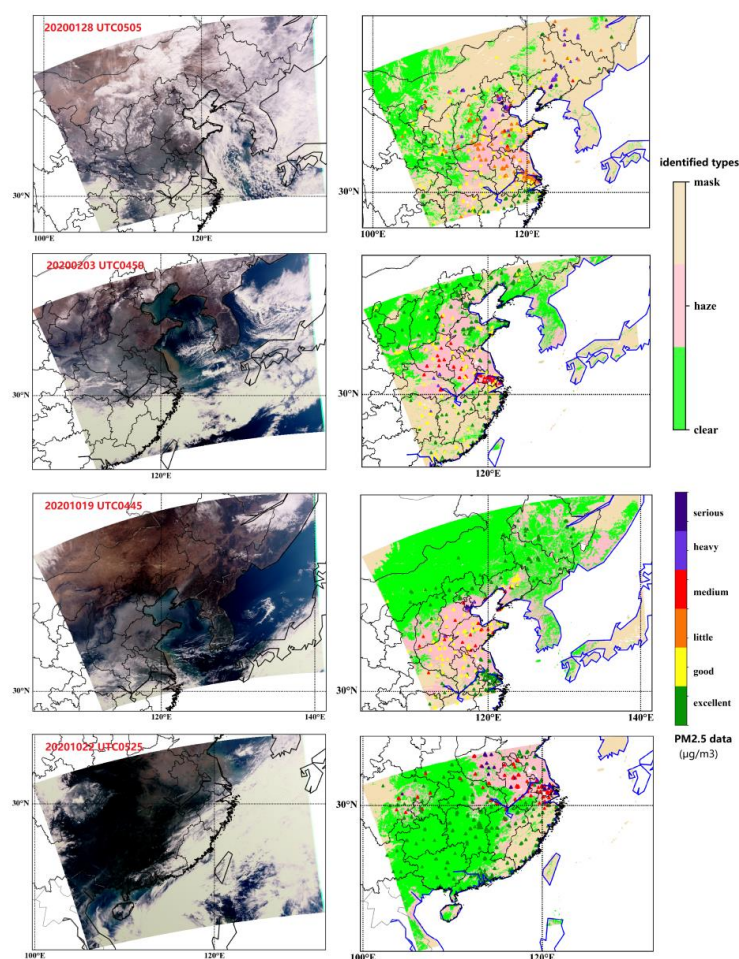


Figure 10. True color map and identified distribution overlaid with the national $PM_{2.5}$ monitoring data (unit: $\mu\text{g}/\text{m}^3$). $PM_{2.5}$ values belonging to excellent, good, little pollution, medium pollution, heavy pollution and serious pollution are marked as green, yellow, orange, red, purple and dark purple, respectively.

3.3. Cross-Comparison with Other Method

To further demonstrate the accuracy of this analysis, four MERSI orbits were selected, and the identification method proposed by Yang (2022) was implemented in this section for a cross-comparison [23]. On one hand, the pixel identification can provide the distri-

bution of haze regions from a qualitative perspective, and on the other hand, this study's identification results can be used as a haze mask for the retrieval of aerosol quantitative data. That is to say, we should pay more attention to the pixels classified as haze and the number of the pixels that are to be retrieved. Therefore, the cloud, ice/snow and inland waterbody pixels were combined in a background mask, and the remaining pixels were used for the comparison. Figure 11 shows the true color map and the comparisons of two recognition methods on UTC0540 8 November 2019, UTC0445 29 January 2020, UTC0545 31 January 2020 and UTC0550 31 January 2020, covering clear regions over bright surfaces, haze regions over the China North Plain and clear regions in southern China, respectively. It is obviously seen that, both this study and Yang's study (2022) can identify the certainly cloudy pixels well, but there have some discrepancies between them in the identification of cloud edges, heavy haze and clear regions over bright surfaces. For example, the recognition procedure of cloud pixels in Yang's study (2022) is stricter than that of this study, as shown in 29 January 2020, when most of the areas were covered by a haze layer, and the east of Shandong Province was covered by a mixture of haze and clouds [23]. By contrast, our identification method is very sensitive to these phenomena, which is beneficial to increase the number of retrieved pixels and improve the detection ability of the MERSI instrument during haze days. At UTC0550, on 31 January 2020, the number of clear pixels in outer Mongolia detected by Yang (2022) was smaller than that of this study, which was closer to the true color map [23]. It is also found that this study is very sensitive to the identification of cloud edges/clear sky edges, such as those in the eastern part of Yunnan province shown in UTC0545 on 31 January 2020. Although it performs well in the identification of haze or clear or cloud edges, large errors will be introduced in the aerosol retrievals. This is a double-edged sword that needs to be balanced in different application scenarios.

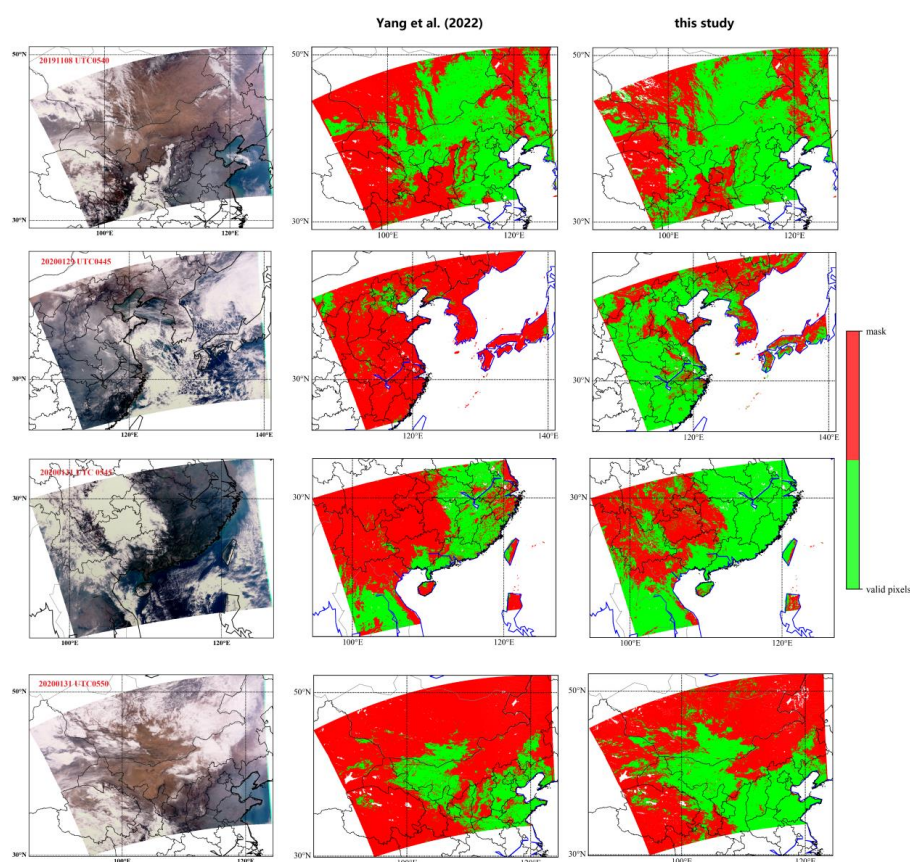


Figure 11. True color map and comparison of identified results of Yang (2022) [23] and the MHAM algorithm at UTC0540 on 8 October 2019 (the first line), UTC0445 on 29 January 2020, UTC0545 on 31 January 2020 and UTC0550 on 31 January 2020.

4. Conclusions

Cloud detection products based on FY3D/MERSI-II data have been released as operational products for many years, supplying cloud masks for the improved retrieval of atmospheric environmental products (such as aerosol and PM_{2.5}, etc.), and they have continental surface parameters (such as the land surface temperature). For aerosol quantitative retrieval, the cloud detection products of MERSI have limits in their haze area identification. The absolutely clear and cloudy pixels can be distinguished from each other based on the fact that they have opposite characteristics in terms of reflectance in the visible channels and brightness temperature in the infrared channels. Combined with the actual patterns of the MERSI L1 data, the positive corresponding relationship between the apparent reflectance at 0.865 μm and 1.64 μm for the clear pixels over regions with a bright surface is proposed as an identification condition. Thus, this study proposes a novel MERSI haze mask (MHAM) algorithm that divides the pixels into one of three categories: cloudy, clear or haze ones, thereby resolving the problem of distinguishing haze pixels from the clear ones over a bright surface.

In comparing the operational Aqua/MODIS and MERSI-II cloud detection products with the true color map, it reveals that these two products misclassified the heavy haze pixels as certain cloud, possible cloud and possible clear pixels, and they misclassified the pixels with light/moderate haze conditions as possible cloud, possible clear and certainly clear regions. In contrast, the novel algorithm proposed in this paper is able to capture the haze regions correctly, making it more compatible with the true color images. The real-time PM_{2.5} data from the national air quality monitoring stations served as true values, and two thresholds were used to evaluate the new algorithm. The results showed that the novel algorithm has 72.22% (13 out of total 18 samples) accuracy when a PM_{2.5} that was larger than 35 $\mu\text{g}/\text{m}^3$ was considered as haze conditions, while for PM_{2.5} values that were larger than 50 $\mu\text{g}/\text{m}^3$, 83.33% and 66.67% of the total samples were examined with better identification rates than 85% and 90%, respectively, indicating that the greater the ground-based PM_{2.5} value is, the better the consistency is in satellite haze identification. Through the cross-comparison with the method proposed by Yang (2022) [23], it was found that the novel algorithm has a better sensitivity to bright surface clear sky areas and haze areas, and there will be more valid pixels when the subsequent quantitative inversion of aerosol characteristics is performed.

Haze detection based on satellite remote sensing data is still in the research stage of recognition, and there has been no corresponding official product released so far, thus leading to great difficulties in the quantitative validation of the haze identification effect. With the definition of haze, a richer comparison between the accuracies of this identification method by using combining relative humidity and visibility data will be carried out. In addition, the haze identification method proposed in this study directly depends on the apparent reflectance and brightness temperature, that is, when the calibration coefficient is adjusted, the corresponding identification threshold also needs to be updated synchronously. We will monitor of the MERSI instrument data state and update the recognition threshold iteratively.

Author Contributions: Conceptualization, Y.S. and X.Z.; methodology, Y.S. and L.C.; software, Y.S.; validation, Y.S. and L.Y.; investigation, Y.S. and F.W.; resources, Y.S.; data curation, L.C., F.W., N.X.; writing—original draft preparation, Y.S.; writing—review and editing, L.C., Z.Z., L.Y., F.W., N.X. and X.Z.; visualization, Y.S.; supervision, L.C., N.X. and X.Z.; project administration, Y.S., F.W., L.C.; funding acquisition, Y.S. and F.W. All authors have read and agreed to the published version of the manuscript.

Funding: This work is jointly supported by the National Key Research and Development Program of China (No. 2019YFC0214601) and Beijing Municipal Natural Science Foundation (No. 8214065).

Data Availability Statement: Data sharing not applicable.

Acknowledgments: We appreciate the NASA Langley Research Center Atmospheric Sciences Data Center (<https://eosweb.larc.nasa.gov/>, accessed by 10 April 2022) for providing the MYD35 product.

Conflicts of Interest: The authors declare no conflict of interest.

References

1. Wu, D. A Discussion on Difference between Haze and Fog and Warning of Ash Haze Weather. *Meteorol. Mon.* **2005**, *31*, 7.
2. Gautam, R.; Hsu, N.C.; Eck, T.F.; Holben, B.N.; Janjai, S.; Jantarach, T.; Tsay, S.C.; Lau, W.K. Characterization of aerosols over the Indochina peninsula from satellite-surface observations during biomass burning pre-monsoon season. *Atmos. Environ.* **2013**, *78*, 51–59. [[CrossRef](#)]
3. Menon, S.; Hansen, J.; Nazarenko, L.; Luo, Y.F. Climate effects of black carbon aerosols in China and India. *Science* **2002**, *297*, 2250–2253. [[CrossRef](#)] [[PubMed](#)]
4. Zhang, X.Y.; Wang, F.; Wang, W.H.; Huang, F.X.; Chen, B.L.; Gao, L.; Wang, S.P.; Yan, H.H.; Ye, H.H.; Si, F.Q.; et al. The development and application of satellite remote sensing for atmospheric compositions in China. *Atmos. Res.* **2020**, *245*, 105056. [[CrossRef](#)]
5. Xia, X.A.; Chen, H.B.; Wang, P.C.; Zhang, W.X.; Goloub, P.; Chatenet, B.; Eck, T.F.; Holben, B.N. Variation of column-integrated aerosol properties in a Chinese urban region. *J. Geophys. Res.-Atmos.* **2006**, *111*. [[CrossRef](#)]
6. Liu, X.G.; Li, J.; Qu, Y.; Han, T.; Hou, L.; Gu, J.; Chen, C.; Yang, Y.; Liu, X.; Yang, T.; et al. Formation and evolution mechanism of regional haze: A case study in the megacity Beijing, China. *Atmos. Chem. Phys.* **2013**, *13*, 4501–4514. [[CrossRef](#)]
7. Zhang, X.; Wang, H.; Che, H.Z.; Tan, S.C.; Shi, G.Y.; Yao, X.P. The impact of aerosol on MODIS cloud detection and property retrieval in seriously polluted East China. *Sci. Total Environ.* **2020**, *711*, 134634. [[CrossRef](#)] [[PubMed](#)]
8. Che, H.; Xia, X.; Zhu, J.; Li, Z.; Dubovik, O.; Holben, B.; Goloub, P.; Chen, H.; Estelles, V.; Cuevas-Agullo, E.; et al. Column aerosol optical properties and aerosol radiative forcing during a serious haze-fog month over North China Plain in 2013 based on ground-based sunphotometer measurements. *Atmos. Chem. Phys.* **2014**, *14*, 2125–2138. [[CrossRef](#)]
9. Cheng, Z.; Wang, S.; Fu, X.; Watson, J.G.; Jiang, J.; Fu, Q.; Chen, C.; Xu, B.; Yu, J.; Chow, J.C.; et al. Impact of biomass burning on haze pollution in the Yangtze River delta, China: A case study in summer 2011. *Atmos. Chem. Phys.* **2014**, *14*, 4573–4585. [[CrossRef](#)]
10. Tao, M.H.; Chen, L.F.; Wang, Z.F.; Wang, J.; Tao, J.H.; Wang, X.H. Did the widespread haze pollution over China increase during the last decade? A satellite view from space. *Environ. Res. Lett.* **2016**, *11*, 054019. [[CrossRef](#)]
11. Tao, M.H.; Chen, L.F.; Xiong, X.Z.; Zhang, M.G.; Ma, P.F.; Tao, J.H.; Wang, Z.F. Formation process of the widespread extreme haze pollution over northern China in January 2013: Implications for regional air quality and climate. *Atmos. Environ.* **2014**, *98*, 417–425. [[CrossRef](#)]
12. Tao, M.H.; Li, R.; Wang, L.L.; Lan, F.; Wang, Z.F.; Tao, J.H.; Che, H.Z.; Wang, L.C.; Chen, L.F. A critical view of long-term AVHRR aerosol data record in China: Retrieval frequency and heavy pollution. *Atmos. Environ.* **2020**, *223*, 117246. [[CrossRef](#)]
13. Lim, H.; Choi, M.; Kim, J.; Kasai, Y.; Chan, P.W. AHI/Himawari-8 Yonsei Aerosol Retrieval (YAER): Algorithm, Validation and Merged Products. *Remote Sens.* **2018**, *10*, 699. [[CrossRef](#)]
14. Remer, L.A.; Mattoo, S.; Levy, R.C.; Heidinger, A.; Pierce, R.B.; Chin, M. Retrieving aerosol in a cloudy environment: Aerosol product availability as a function of spatial resolution. *Atmos. Meas. Tech.* **2012**, *5*, 1823–1840. [[CrossRef](#)]
15. Wang, Y.; Chen, L.F.; Li, S.S.; Wang, X.H.; Yu, C.; Si, Y.D.; Zhang, Z.L. Interference of Heavy Aerosol Loading on the VIIRS Aerosol Optical Depth (AOD) Retrieval Algorithm. *Remote Sens.* **2017**, *9*, 397. [[CrossRef](#)]
16. Zeng, S.; Parol, F.; Riedi, J.; Cornet, C.; Thieuleux, F. Examination of POLDER/PARASOL and MODIS/Aqua Cloud Fractions and Properties Representativeness. *J. Clim.* **2011**, *24*, 4435–4450. [[CrossRef](#)]
17. Levy, R.C.; Mattoo, S.; Munchak, L.A.; Remer, L.A.; Sayer, A.M.; Patadia, F.; Hsu, N.C. The Collection 6 MODIS aerosol products over land and ocean. *Atmos. Meas. Tech.* **2013**, *6*, 2989–3034. [[CrossRef](#)]
18. Hutchison, K.D.; Iisager, B.D.; Kopp, T.J.; Jackson, J.M. Distinguishing aerosols from clouds in global, multispectral satellite data with automated cloud classification algorithms. *J. Atmos. Ocean. Technol.* **2008**, *25*, 501–518. [[CrossRef](#)]
19. Ge, W.; Chen, L.F.; Si, Y.D.; Ge, Q.; Fan, M.; Li, S.S. Haze Spectral Analysis and Detection Algorithm Using Satellite Remote Sensing Data. *Spectrosc. Spectr. Anal.* **2016**, *36*, 3817–3824.
20. Shang, H.Z.; Chen, L.F.; Tao, J.H.; Su, L.; Jia, S.L. Synergetic Use of MODIS Cloud Parameters for Distinguishing High Aerosol Loadings from Clouds Over the North China Plain. *IEEE J. Sel. Top. Appl. Earth Obs. Remote Sens.* **2014**, *7*, 4879–4886. [[CrossRef](#)]
21. Ackerman, S.A.; Strabala, K.I.; Menzel, W.P.; Frey, R.A.; Moeller, C.C.; Gumley, L.E. Discriminating clear sky from clouds with MODIS. *J. Geophys. Res.-Atmos.* **1998**, *103*, 16. [[CrossRef](#)]
22. Shang, H.Z.; Chen, L.F.; Letu, H.S.; Zhao, M.; Li, S.S.; Bao, S.H. Development of a daytime cloud and haze detection algorithm for Himawari-8 satellite measurements over central and eastern China. *J. Geophys. Res.-Atmos.* **2017**, *122*, 3528–3543. [[CrossRef](#)]
23. Yang, L.K.; Hu, X.Q.; Wang, H.; He, X.W.; Liu, P.; Xu, N.; Yang, Z.D.; Zhang, P. Preliminary test of quantitative capability in aerosol retrieval over land from MERSI-II onboard FY3D. *Natl. Remote Sens. Bull.* **2022**, *26*, 923–940.
24. Shi, Y.X.R.; Levy, R.C.; Yang, L.K.; Remer, L.A.; Mattoo, S.; Dubovik, O. A Dark Target research aerosol algorithm for MODIS observations over eastern China: Increasing coverage while maintaining accuracy at high aerosol loading. *Atmos. Meas. Tech.* **2021**, *14*, 3449–3468. [[CrossRef](#)]

25. Yang, Z.D.; Lu, N.M.; Shi, J.M.; Zhang, P.; Dong, C.H.; Yang, J. Overview of FY-3 Payload and Ground Application System. *IEEE Trans. Geosci. Remote Sens.* **2012**, *50*, 4846–4853. [[CrossRef](#)]
26. Hu, X.Q.; Liu, J.J.; Sun, L.; Rong, Z.G.; Li, Y.; Zhang, Y.; Zheng, Z.J.; Wu, R.H.; Zhang, L.J.; Gu, X.F. Characterization of CRCS Dunhuang test site and vicarious calibration utilization for Fengyun (FY) series sensors. *Can. J. Remote Sens.* **2010**, *36*, 566–582. [[CrossRef](#)]
27. Hu, X.Q.; Sun, L.; Liu, J.J.; Ding, L.; Wang, X.H.; Li, Y.; Zhang, Y.; Xu, N.; Chen, L. Calibration for the Solar Reflective Bands of Medium Resolution Spectral Imager Onboard FY-3A. *IEEE Trans. Geosci. Remote Sens.* **2012**, *50*, 4915–4928. [[CrossRef](#)]
28. Xu, N.; Niu, X.H.; Hu, X.Q.; Wang, X.H.; Wu, R.H.; Chen, S.S.; Chen, L.; Sun, L.; Ding, L.; Yang, Z.D.; et al. Prelaunch Calibration and Radiometric Performance of the Advanced MERSI II on FengYun-3D. *IEEE Trans. Geosci. Remote Sens.* **2018**, *56*, 4866–4875. [[CrossRef](#)]
29. Chen, J.; Yao, Q.; Chen, Z.Y.; Li, M.C.; Hao, Z.Z.; Liu, C.; Zheng, W.; Xu, M.Q.; Chen, X.; Yang, J.; et al. The Fengyun-3D (FY-3D) global active fire product: Principle, methodology and validation. *Earth Syst. Sci. Data* **2022**, *14*, 3489–3508. [[CrossRef](#)]
30. Li, C.C.; Mao, J.T.; Lau, A.K.H.; Yuan, Z.B.; Wang, M.H.; Liu, X.Y. Application of MODIS satellite products to the air pollution research in Beijing. *Sci. China Ser. D Earth Sci.* **2005**, *48*, 209–219.
31. Li, S.S.; Chen, L.F.; Xiong, X.Z.; Tao, J.H.; Su, L.; Han, D.; Liu, Y. Retrieval of the Haze Optical Thickness in North China Plain Using MODIS Data. *IEEE Trans. Geosci. Remote Sens.* **2013**, *51*, 2528–2540. [[CrossRef](#)]
32. Sayer, A.M.; Hsu, N.C.; Bettenhausen, C.; Jeong, M.J. Validation and uncertainty estimates for MODIS Collection 6 “Deep Blue” aerosol data. *J. Geophys. Res.-Atmos.* **2013**, *118*, 7864–7872. [[CrossRef](#)]
33. Xiao, Q.; Zhang, H.; Choi, M.; Li, S.; Kondragunta, S.; Kim, J.; Holben, B.; Levy, R.C.; Liu, Y. Evaluation of VIIRS, GOCI, and MODIS Collection 6AOD retrievals against ground sunphotometer observations over East Asia. *Atmos. Chem. Phys.* **2016**, *16*, 1255–1269. [[CrossRef](#)]
34. You, W.; Zang, Z.L.; Pan, X.B.; Zhang, L.F.; Chen, D. Estimating PM_{2.5} in Xi’an, China using aerosol optical depth: A comparison between the MODIS and MISR retrieval models. *Sci. Total Environ.* **2015**, *505*, 1156–1165. [[CrossRef](#)] [[PubMed](#)]
35. Wang, Z.; Li, R.Y.; Chen, Z.Y.; Yao, Q.; Gao, B.B.; Xu, M.Q.; Yang, L.; Li, M.C.; Zhou, C.H. The estimation of hourly PM_{2.5} concentrations across China based on a Spatial and Temporal Weighted Continuous Deep Neural Network (STWC-DNN). *ISPRS J. Photogramm. Remote Sens.* **2022**, *190*, 38–55. [[CrossRef](#)]

Disclaimer/Publisher’s Note: The statements, opinions and data contained in all publications are solely those of the individual author(s) and contributor(s) and not of MDPI and/or the editor(s). MDPI and/or the editor(s) disclaim responsibility for any injury to people or property resulting from any ideas, methods, instructions or products referred to in the content.